nature communications

Article

https://doi.org/10.1038/s41467-025-67785-3

Connectivity of the adult human brain with sequential neurogenesis of circuits and transcriptomics signatures

Received: 27 June 2022

Accepted: 9 December 2025

Published online: 31 December 2025

Check for updates

Ibai Diez[1,2,3,4,14], Fernando García-Moreno[4,5,6,14], Nayara Carral-Sainz[7], Sebastiano Stramaglia[8], Alicia Nieto-Reyes[9], Mauro D'Amato[4,10,11], Jesús M Cortes[3,4,12] & Paolo Bonifazi[3,4,13]

Understanding the architectural principles that shape human brain networks is a major challenge for systems neuroscience. We hypothesize that the centrality of the different brain circuits in the human connectome is a product of their embryogenic age, such that early-born nodes should become stronger hubs than those born later. Using a human brain segmentation based on embryogenic age, we observed that nodes' structural centrality correlated with their embryogenic age, supporting our hypothesis. An opposite trend was found at functional level. The difference in embryonic age between nodes inversely correlated with the probability of existence of links and their weights. Brain transcriptomic analysis revealed strong associations between embryonic age, structure-function centrality, and the expression of genes related to nervous system development, synapse regulation and human neurological diseases. Our results highlight two key principles regarding the wiring of the human brain: older-get-richer rule, whereby earlier-born regions become network hubs, and a preferential-age-attachment rule, whereby regions preferentially connect to others with similar neurogenic timing.

The most characteristic anatomical property of brain networks is their organization across multiple spatial scales. Micro-scale neurons are interconnected within local circuits or microdomains, which are scaled up to the macro-scale over which long-range connections allow distant neurons to communicate and different circuits to interact[1,2]. Consequently, a key challenge in fundamental and clinical neuroscience is to decipher the rules of connectivity that shape brain networks in order to understand how the brain works and how traumatic or neurological damage may affect brain functionality[3].

The general structure and function of the human brain, and its internal connectivity are all the result of its developmental history, which is at the same time the product of evolution[4]. As such, the brain follows developmental instructions to establish a blueprint of diverse neural connections, the functioning of which can be later refined.

[1]Center for Inflammation Imaging, Department of Radiology, Massachusetts General Hospital, Harvard Medical School, Boston, MA, USA. [2]Athinoula A. Martinos Center for Biomedical Imaging, Department of Radiology, Massachusetts General Hospital, Harvard Medical School, Charlestown, MA, USA. [3]Computational Neuroimaging Lab, Biobizkaia Health Research Institute, Barakaldo, Spain. [4]IKERBASQUE: The Basque Foundation for Science, Bilbao, Spain. [5]Achucarro Basque Center for Neuroscience, Scientific Park of the University of the Basque Country (UPV/EHU), Leioa, Spain. [6]Department of Neuroscience, Faculty of Medicine and Odontology, UPV/EHU, Barrio Sarriena s/n, Leioa, Bizkaia, Spain. [7]Departamento de Ciencias de la Tierra y Física de la Materia Condensada, Facultad de Ciencias, Universidad de Cantabria, Santander, Spain. [8]Dipartimento Interateneo di Fisica, Università degli Studi di Bari Aldo Moro, and INFN, Sezione di Bari, Bari, Italy. [9]Departamento de Matemáticas, Estadística y Computación, Facultad de Ciencias, Universidad de Cantabria, Santander, Spain. [10]Department of Medicine and Surgery, LUM University, Casamassima, Italy. [11]Gastrointestinal Genetics Lab, CIC bioGUNE - BRTA, Derio, Spain. [12]Department of Cell Biology and Histology, University of the Basque Country (UPV/EHU), Leioa, Spain. [13]Department of Physics and Astronomy, University of Bologna, Bologna, Italy. [14]These authors contributed equally: Ibai Diez, Fernando García-Moreno. e-mail: paol.bonifazi@gmail.com

Previous studies have evaluated the development of brain networks at different stages of maturation, particularly in relation to the appearance of key network structures like central nodes[5]. However, there are still no detailed studies that fully relate the connectivity of the adult human brain with the sequential (evolutionarily preserved) neurogenesis of circuits.

Complex networks have emerged over the past two decades and provide a powerful mathematical framework to quantify the complexity of brain circuitries. Different studies that assessed the data from real-world networks' have highlighted that small-world, scale-free or heavy-tailed distribution network organizations are stereotypic topologies of many distinct domains[6,7]. These key topologies have been identified at the structural-functional level in micro-circuits, and in meso- and macro-scale networks[8]. A pioneering study[9] showed that the principle the rich gets richer (a.k.a. preferential attachment) led to the development of the scale-free networks that are characterized by highly connected rare nodes or hubs. According to this principle, when a new node attaches to the network, it will preferably establish links to nodes which are already rich in connections, therefore making them richer. An earlier work showed evidence that, at micro-circuit level in the brain, hippocampal GABAergic neuronal functional hubs were the early-born GABAergic neurons in both developing and adult murine circuits[10–12].

Inspired by this model[9], we seek to test if earlier micro-circuit evidence also extrapolates to the macro-scale whole brain connectivity combining the heavy-tailed signatures widely observed in brain networks with the stereotypic, evolutionary-preserved sequential neurogenesis in the developing brain. Here we show that functional and structural brain networks are shaped according to the rule that the older gets richer, i.e., the evolutionary older circuits or those generated earlier in embryogenesis are those most central in the organization of the adult brain network[13]. We show that the hubness of brain circuits, based on metrics of centrality in complex networks, strongly correlates with embryogenic age and further connect this findings to underlying molecular mechanism.

Results

Sequential neurogenesis, brain segmentation and connectivity

To test our hypothesis, we differentiated and segmented human brain circuits according to their First neurogenic Time (FirsT) following the criteria established in the methods, i.e., the post-conception day (or embryonic day) on which the first neurons of the circuit are generated in the corresponding developmental neuromere (Fig. 1A). The match between developmental neuromeres and adult circuits, and the estimation of FirsT in humans extrapolated from different animal species, is presented with underlying literature and full references in the Method section. As such, a list was generated that organized the human circuits according to their FirsT, from older to younger circuits (Table 1). We identified 18 distinct macro-circuits (MACs; atlases used for the different MACs are listed in supplementary table 1) corresponding to 18 separated fundamental developmental units for which a timing sequence based on their FirsT could be defined. Other relevant circuits for which detailed developmental information is known could not be segmented on MRI, such as the neocortical layers and thalamic nuclei (see Supplementary Information). Regarding the latter point, an important limitation of this study pertains to the neocortex, which constitutes the majority of the human brain's volume. The information about the neocortex was inferred from animals with less significant cortical relevance. Specifically, we derived cortical measures of FirsT from animal models representing four key cortical circuits: frontal, parietal, temporal, and occipital cortex. These circuits correspond to the sequence of their first neurogenesis. While we acknowledge the possibility of more subtle variations in neurogenesis gradients within these cortical regions in humans across gestational weeks[14], no precise and available data or quantification exist for humans. Nonetheless, we have confidence in extrapolating data from extensively studied animal models, such as rodents and primates. It is important to consider that the pace of neurogenesis differs between these species; the initial neurogenesis of cortical areas (referred to as FirsT neurogenesis) differs approximately 6 days in humans, which is roughly the overall duration of murine cortical neurogenesis, as indicated in Table 1. We used dMRI and resting-state fMRI images acquired at 7 T from $N = 184$ healthy subjects taken from the Human Connectome project to reconstruct structural-functional brain networks (see Fig. 1B and Methods). Since the volume of the different MACs spanned more than two orders of magnitude (see Supplementary Fig. 1B), the MACs were also parcellated (see Methods) to obtain spatially segregated ROIs with a volume comparable to the smallest circuits (e.g., the Locus Coeruleus -LC), each in the range of several dozen voxels (see Supplementary Fig. 1A for the overall ROI volume distribution and Table 1 for the number of ROIs per MAC). Similar parcellations with more than two thousands microregions have previously used for brain connectivity studies[15–19].

Each of the 18 MACs had a corresponding FirsT, which was also assigned to all ROIs obtained for a given MAC, and a total of 2566 ROIs were defined in the brain. The structural and functional connectivity between the ROIs (we refer to as SC and FC respectively) were calculated and represented as matrices (Fig. 1B and Fig. 2A). The networks were calculated from the average of all the subjects, based on probabilistic tractography and resting-state activity correlations. Note that only positive functional links with significant correlations (i.e., passing the Bonferroni multiple-comparison correction, see Methods) were considered, finally leading to a functional network connectivity density of 6.5%. A similar density level was obtained in the structural networks by thresholding probabilistic tractography consistently with previous studies (18; see Methods). Finally, the possible existence of patterns of correlation between ROIs/MAC connectivity and FirsT was explored via networks' centrality (hubness) measurements. In addition, the brain maps of FirsT and nodes' hubness were related to the brain maps of the transcriptome of 20787 coding-genes (Fig. 1C), in order to obtain a complementary biological correlate to the brain connectivity model.

To quantify the centrality of each ROI and MAC (represented by the average strength of the englobed ROIs) in the brain networks as function of FirsT (Fig. 2A), we calculated the eigenvector centrality (EC) for each ROI (see violin plots in Fig. 2A) and the global MAC strength (G-st, derived from a 18 x 2566 connectivity matrix, obtained as average of ROIs' link weights within a MAC, see scatter plots in Fig. 2B and Methods).

Node centrality versus sequential neurogenesis: the "older gets richer"

To test our main hypothesis, i.e. that the structural centrality of brain nodes is inversely correlated with embryogenic age, such that the earlier the FirsT the higher the centrality, we computed the Spearman's partial correlation (SP-pCorr) between the EC and FirsT, eliminating the effect of the cofounder white matter volume per ROI or MAC (i.e. averaged across ROIs) that also shows a gradient between early and late generated structures (Supplementary Fig. 1 left plot). Similarly, we repeated the same calculation for the functional networks, in this case removing the cofounder of gray matter volume per ROI or MAC (Supplementary Fig. 1 right plot). The plots of the EC obtained for the SC and FC are displayed in Fig. 2B.

The ROIs' EC of the SC and FC nodes showed significant trends with FirsT, respectively with negative (SP-pCorr = −0.44, $p = 0.003$) and positive (SP-pCorr=0.34, $p = 0.018$) correlations. When looking at the overall centrality of the MACs, we observed for the G-st a negative correlation with respect to FirsT for the SC (SP-pCorr = −0.54, $p < 0.03$) and positive correlation for the FC (SP-pCorr =0.78, $p < 0.001$), similarly to what was observed for ROIs. Note that the

https://doi.org/10.1038/s41467-025-67785-3

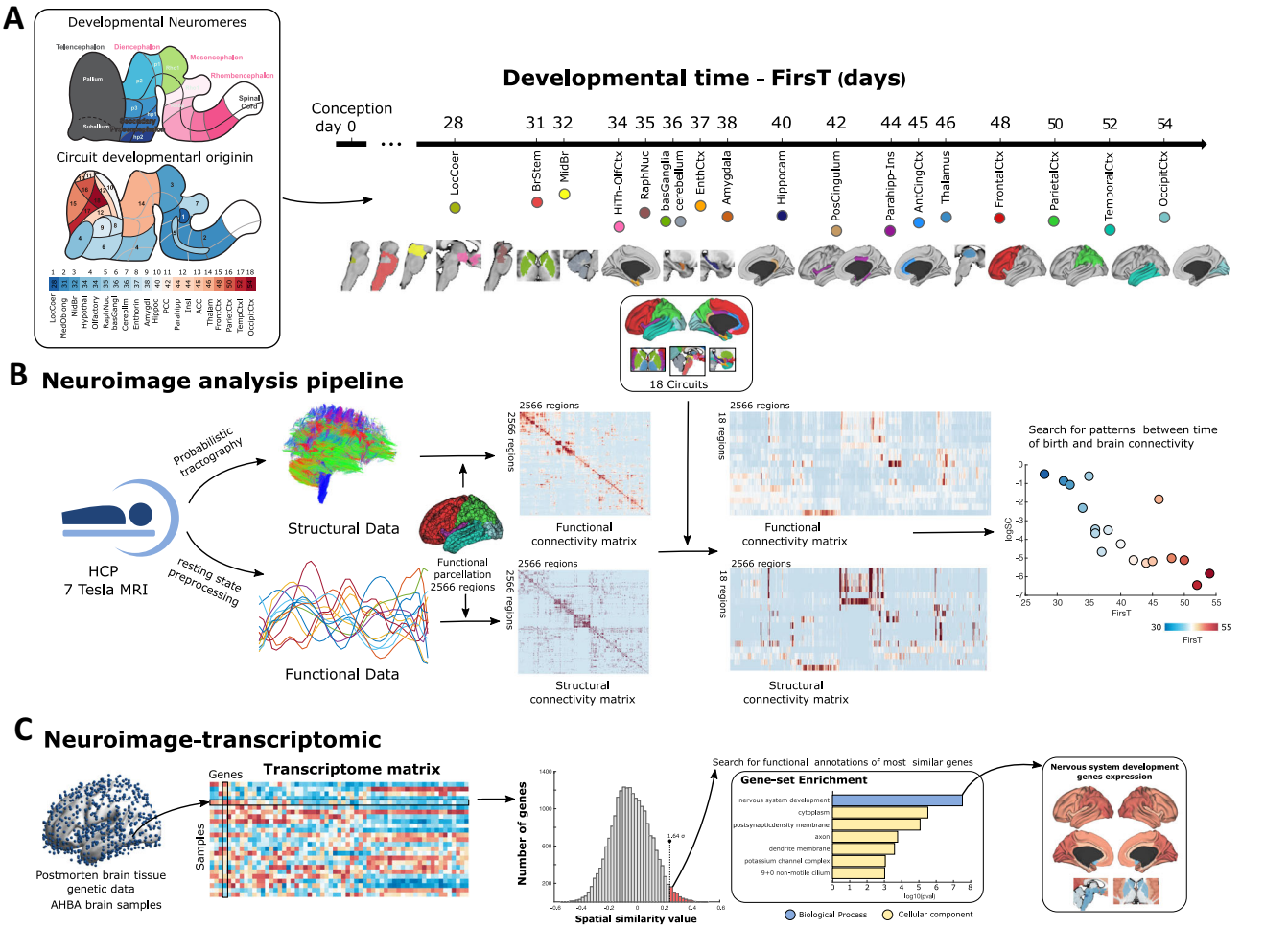

Fig. 1 | From the circuits' embryogenic age to brain networks and transcriptomics. A Sagittal schemes of the early embryonic human brain. The upper scheme represents the neuromeres and fundamental regions of development (different colors are used to differentiate different regions), the lower scheme displays the location of the 18 MACs within the early embryonic human brain, color-coded according to their FirsT. **B** Scheme of the neuroimage analysis pipeline. Brain networks were reconstructed from healthy adult subjects scanned by MRI at 7 T within the HCP initiative. For each subject, the structural and functional networks were reconstructed using probabilistic tractography and resting-state activity, respectively. For every pair of ROIs (2566 ROIs), the structural connectivity matrix represents the putative number of fibers connecting them, while the functional connectivity matrix reports the correlation in their activity as revealed by the BOLD time series. The averages across subjects were used as final representative brain networks (see Methods). From the 2566 ROIs' matrices, the 18 × 2566 MACs' connectivity matrices were reconstructed and represents the average weights of the links connecting the ROIs within the MAC to the rest of the brain ROIs (see Methods). To identify patterns between networks' topology and neurogenesis, the correlation between the nodes' centrality and embryonic age was calculated. **C** Brain transcriptome data from AHBA dataset (see methods) was used to search for protein coding genes with a high similarity between its spatial brain expression and embryonic age. Functional annotations of the obtained genes were further computed using overrepresentation analysis to find significantly associated biological processes and cellular components associated with embryonic age. MATLAB (MathWorks, Inc.) was used for the computational analysis and plotting shown in this figure.

negative correlations observed for the SC (physically constrained spatial domain) support the leading hypothesis that early born brain regions (e.g., the LC and brainstem) have greater "hubness" or centrality, we refer to this as "the older gets richer" principle. By contrast, in the case of the FC (functional domain related to time and dynamics) the positive correlations observed between centrality and FirsT highlight the greater functional centrality of late brain circuits (such as neocortical ones).

The opposite trends of the MACs' centrality in respect to their time of birth can be visualized on a brain surface (Fig. 3A).

Connectivity versus sequential neurogenesis: the "age preferential attachment"

We next checked whether the difference in the time of neurogenesis (ΔFirsT) might also be related to the probability of the existence and the weight of the links (Fig. 2C). In the SC and FC, where a connection was present in 5% and 6.5% of the overall node pairs respectively (see Methods), the link probability decreased as a function of ΔFirsT with a Spearman correlation of −0.53 ($p < 0.01$) and −0.94 ($p < 10^{-10}$). Similarly, the link weight decreased with a correlation of −0.74 ($p < 0.001$) and −0.87 ($p < 10^{-5}$). The plots of the average links' weight connecting ROIs belonging to different MACs (global link weight, see Methods) shown in Supp. Figure 3. and Supp. Figure 4 for each MAC separately, provide a visualization of how the brain circuits generated at similar neurogenic time points tend to connect more strongly. We refer to this as the preferential age attachment principle. As an example, the structural connectivity of three representative MACs was visualized over a linear time scale, relative to the earliest (Locus Coeruleus, 28 days), latest (occipital cortex, FirsT 54 days) and intermediate FirsT (hippocampus, 40 days: Fig. 3B1–3). This visualization shows that the links' weights of the earliest MAC are much higher than that of the later MACs, and for the case of the LC and hippocampus, it also shows that brain circuits

https://doi.org/10.1038/s41467-025-67785-3

Table 1 | Developmental information of the human brain macrocircuits studied

	Major developmental brain area	Circuit (abbreviation)	fMRI Comprised structures	Translated earliest stage in humans (embryonic days)	Earliest stage in other species	Source	Observations	ROIs #
1	Rhombencephalon	Locus Coeruleus (LoCo)	Locus Coeruleus	28	Rat - Soon before E12; Mouse - E9	Altman and Bayer, 1980a,b,c; Steindler and Trosko, 1989	Likely one of the earliest generated nucleus. Noradrenergic neuronsare the earliest-born within the LC	2
2	Rhombencephalon	Medulla Oblongata (MeOb)	Pons and Medulla oblongata	31	Rat - Soon after 12	Altman and Bayer, 1980a	Brainstem neurogenesis starts much earlier than in the rest of the brain. However we could not segment its many different compartments by fMRI and so it appears fused in one single circuit.	40
3	Mesencephalon	Midbrain (MidB)	Superior colliculus, inferior colliculus, tegmental midbrain	32	Mouse - E10.5	Bayer et al., 1995;Achim et al., 2012	Substantia nigra pars reticulata is the earliest mesencephalic nucleus to start neurogenesis	23
4	Seconary Prosencephalon	Hypothalamus (HpTh)	Hypothalamus, mammilary bodies	34	Rat - E12;Macaque - E33;Cat - E21	Altman and Bayer, 1978a,b;Eerdenburg and Rakic, 1994; translatingtime.org	Lateral hypothalamic nuclei (lateral hypothalamic nucleus, lateral preoptic area and lateral mammilary bodies) start hypothalamic neurogenesis at	18
	Telencephalon	Olfactory (OlfC)	Olfactory Cortices	34	Mouse E11	translatingtime.org (Workman et al., 2013)	Unique segmentation and ROI identification with Hypothalamus	
5	Rhombencephalon	Raphe Nuclei (RaN)	Raphe nuclei	35	Rat E12		Neurogenesis in the Raphe nuclei starts in the Raphe Magnus nucleus	3
6	Telencephalon	Basal Ganglia (BG)	Caudate, Putamen, Accumbens, Septum	36	Mouse - E11;Macaque - E38	Brand and Rakic, 1980	Accumbens starts neurogenesis at E38 in macaque; Striatum and globus pallidus start soon after.	77
7	Rhombencephalon	Cerebellum (Ceb)	Cerebellar cortex, deep cerebellar nuclei	36	Mouse E11;Rat - E13	Miale and Sidman, 1961; Altman and Bayer, 1978c; Leto et al., 2006	Earliest neurons are projection neruons of the deep cerebellar nuclei, followed by Purkinje neurons.	275
8	Telencephalon	Entorhinal (EntC)	Entorhinal cortex	37	Rat - soon after E14	Bayer, 1980a	Neurogenesis starts earlier to other parahippocampal cortices	11
9	Telencephalon	Amygdala (Amyg)	Pallial amygdala, subpallial amygdala	38	Mouse E11	McConnell and Angevine, 1983; Soma et al., 2009	Neurogenesis starts with GABAergic populations of central and medial nuclei, followed by the glutamatergic neurons of the baso-lateral complex	8
10	Telencephalon	Hippocampus (Hip)	Amon horn, Dentate gyrus	40	Rat E14.5	Bayer, 1980a	Earliest neurons occupy the superficial and deep layers of the Ammon´s horn (CA1 to CA3), and the hilus	21
11	Telencephalon	Posterior cingulum(PosC)	Posterior cingular cortex	42	Rat E14.5	translatingtime.org	Inferred from translatingtime.org Earlier than the anterior cingulate cortex	22
12	Telencephalon	Parahippocampal cortices (ParH)	Parahippocampal cortex	44	Rat E15	Bayer, 1980a	Includes subiculum and parasubiculum. Unique segmentation and ROI identification with Insula	107
	Telencephalon	Insula (Ins)	Insular cortex	44	Rat E15	Bayer, 1986	First insular neurons occupy the dep layers of the ventral agranular insular cortex.	
13	Telencephalon	Anterior Cingulate cortex (AntC)	Caudal Anterior Cingulate, Rostral Anterior Cingulate	45	Macaque - E40	Granger et al., 1995	First Layer VI neurons in the anterior cingulate cortex were revelaed with	37

https://doi.org/10.1038/s41467-025-67785-3

Table 1 (continued) | Developmental information of the human brain macrocircuits studied

	Major developmental brain area	Circuit (abbreviation)	fMRI Comprised structures	Translated earliest stage in humans (embryonic days)	Earliest stage in other species	Source	Observations	ROIs #
							[3H]-thymidine injection at E40 in the macaque brain	
14	Diencephalon	Thalamus (Thal)	Thalamic nuclei: LP, VL, VPL, LGN, MGN, Pulvinar,	46	Rat - E14	Altman and Bayer, 1979	Several thalamic nuclei (VB, VE, LGN, PO, MGN and LP) start neurogenesis at E14 in the rat brain.	28
15	Telencephalon	Frontal cortex (FroC)	Caudal middle frontal, lateral orbito frontal, medial orbito frontal, paracentral, pars opercularis, pars orbitalis, pars triangularis, precentral, rostral middle frontal, frontal pole and superior frontal cortices	48	Macaque - E40;Ferret - E30;Mouse - E11.5	Rakic, 2002;Reillo and Borrell, 2011;Charvet, 2014;translatingtime.org	Neurogenesis in the cortex starts synchronously throughout all cortical areas. The earliest-generated cortical populations are the Cajal-Retzius cells of the marginal zone and the subplate neurons of layer 6b. Most of these neurons die early after birth, which is why we considered the early generation of deep cortical layers as the onset of a functional cortical neurogenesis.In this layers, there is a gradient of neurogenesis starting first at the rostral pole of the cortex, and finishing last at the caudal regions. In macaque, frontal cortex starts at E45, and occipital cortex starts at E54. In human, we estimate ths gradient as a 2-day difference between cortical lobes.	719
16	Telencephalon	Parietal cortex (ParC)	Inferior parietal, postcentral, precuneus, superior parietal and supramarginal cortices	50				502
17	Telencephalon	Temporal cortex (TemC)	Banks of the Superior Temporal Sulcus, fusiform, inferior temporal, superior temporal, and transverse temporal cortices	52				384
18	Telencephalon	Occipital cortex (OccC)	Cuneus, Lateraloccipital cortex, lingual cortex, pericalcarine cortex	54				289

The table includes the list of 18 MACs, the developmental brain region from which each MAC is derived (see Fig. 1A for location of developmental neuromeres), the main anatomical brain structures contained in each MAC, information about the earliest stage at which neurogenesis (FirsT) is observed or predicted in the human brain, and in other mammalian species, and the number of ROIs in each MAC. References in Supplementary Material.

https://doi.org/10.1038/s41467-025-67785-3

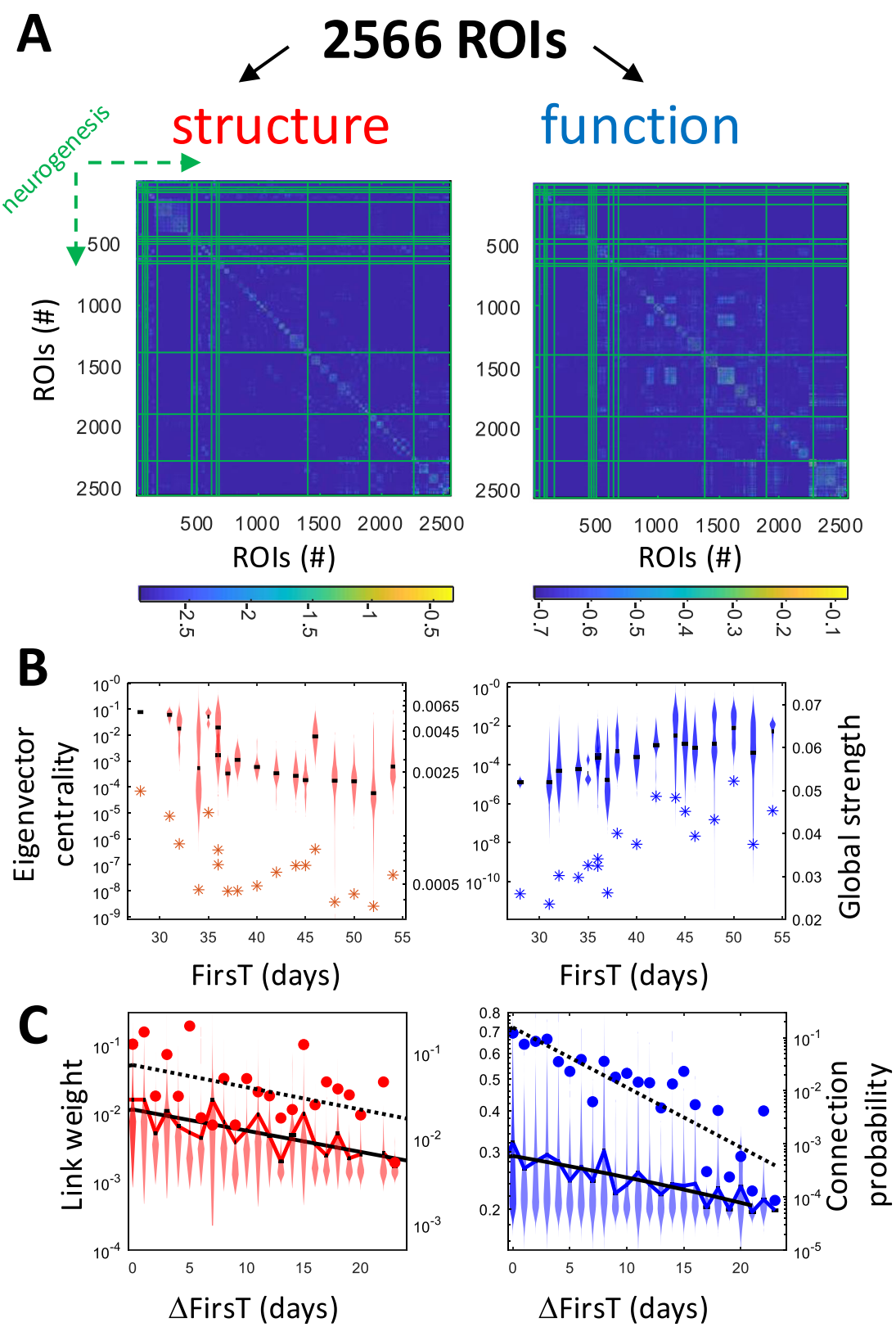

generated at a similar neurogenic time point are more strongly connected.

Transcriptomic signatures of hubness and embryonic age

To dissect how genes' transcription is potentially associated with the brain circuits' FirsT and the brain networks' centrality, post-mortem brain transcriptomic data from the Allen Human Brain Atlas (AHBA) was used. Given the limited spatial sampling across brain regions and donors, we used 90 distinct brain regions with corresponding unique FirsT (supplementary fig. 5), on which gene expression was quantified, and structural and functional centrality was obtained from the average EC of the englobed ROIs (see Methods). The Spearman correlations between the brain maps of expression of 20,737 protein coding genes with FirsT, structural and functional centrality was first separately

Fig. 2 | Scatter plots of the nodes' centrality and the links' probability/weight relative to the FirsT, in structural-functional networks. A Structural and functional networks (SC and FC) composed of the 2566 ROIs are shown on the first and second columns from the left respectively. The green lines separate the 18 different MACs, which are ordered sequentially according to their neurogenesis as shown by the green dotted arrows. Note that the logarithmic values of the structural connectivity matrix are displayed, and in the color-bar the orders of magnitude are marked. **B** Scatter plots of the nodes' centrality as a function of embryonic age. Red and blue indicates the structural and functional cases, respectively. The left y-axis represent the eigenvector centrality of the 2,566 ROIs as violin plots, where the global MAC strength refers to the right y-axis and is plotted with asterisks. **C** Scatter plots of the link weights (left y-axis) as a function of the differences in the first neurogenic birthdate. The colors are as indicated in (**A**). The violin plots for the 2566 ROIs show the link weight distributions while the solid blue/red lines connect their average values. Black solid lines show the exponential (linear) fit on the average values for the structural (functional) case. The link probability is represented by the right y-axes and displayed as dots, and the broken black line shows their exponential fit. All plots have a logarithmic scale in the y-axis. MATLAB (MathWorks, Inc.) was used for the computational analysis and plotting shown in this figure. Source data are provided as a Source Data file.

computed and compared (see scatter plots of Fig. 4A). First, the correlation of gene expression with functional centrality displayed a positive linear trend with respect to the correlation of gene expression with FirsT (Pearson correlation 0.90, $p < 0.01$), while an opposite trend was observed for structural centrality (Pearson correlation −0.72, $p < 0.01$). This observation shows that the expression map of a given gene is similarly correlated to brain maps of FirsT and of functional centrality, in agreement with the fact that FirsT and functional centrality are positively correlated. On the contrary, the negative trend observed when gene expression is correlated to FirsT and to structural centrality is also in agreement with the fact that structural centrality and FirsT are inversely correlated. Further confirmation of what was just described is given by the anti-correlation (Pearson correlation −0.52, $p < 0.01$) observed for gene expression in functional and structural centrality maps.

Next, we performed enrichment analysis on the 1256 genes (6% of the protein coding genes) that were found with a global gene correlation (GGC, i.e., the average of the gene correlations to FirsT, SC and FC EC, see Methods) bigger than 1.64 standard deviations from the distribution obtained (GCC > 0.43; see histogram in Fig. 4A). Gene set enrichment analysis of biological process showed that the genes overrepresented were involved in processes related to development of nervous central system and neuron projection development, and regulation of ion transport, membrane potential, synaptic plasticity and transmission, cell projection organization, insulin secretion, and neurotransmitter levels (Fig. 4B). In addition, different cell components were also overrepresented, such as anchoring junction, voltage-gated potassium channel complexes, dendrites, distal axons, and membranes of synaptic vesicle, pre and post synapses, and neurons (Fig. 4B). Cell type signatures were highly over-represented for several midbrain neurotypes, PFC microglia and astrocytes, and fetal neurons (Fig. 4B). Notably, enrichment of human diseases showed overrepresentation of mental and neurodevelopmental disorders, memory impairment, epilepsy, and other pathologies (Fig. 4B). When performed enrichment only on gene correlation to FirsT (Supplementary Fig. 6), similar results are obtained compared to the use of the global gene correlation that includes functional and structural data.

Additionally, BrainSpan Atlas of the Developing Human Brain[20] was used to investigate if gene expression changes, in the whole brain, across development matched the found genetic patterns using region specific FirsT expression observed with AHBA. The 20,787 genes available in AHBA were divided in 50 bins based on their spatial similarity with FirsT, structural and functional connectivity (Fig. 4B). For each bin the mean slope between developmental time and gene expression across the whole brain in BrainSpan atlas was evaluated. The genes showing higher spatial similarity with FirsT in AHBA were also showing high slope between development time and whole brain expression (blue line in Fig. 4B). The enriched terms for AHBA analysis also showed an increased genetic expression trend with development time (Fig. 4C).

Linking neurogenesis time with disease associated genes

Given these final observations in relation to human diseases, next, we tested and dissected the hypothesis that the genetic contribution to neurological diseases is differentially related to the brain networks' centrality maps and neurogenesis. Therefore, we studied the distribution of the correlation between gene expression, FirsT (Fig. 5 top plots), functional (Fig. 5 middle plots) and structural (Fig. 5 bottom plots) networks' centrality (we refer to these last two cases as the gex-centrality distributions). We expected that genes causally related to neurological disorders would show extreme correlation values (Fig. 5). In particular, we focused on Autism Spectrum Disorder (ASD), Parkinson's disease (PD), Alzheimer's disease (AD) and epilepsy, and we combined two main human gene datasets (see Methods): GeneCards (www.genecards.org) and the Genome-Wide Association Study Catalouge (GWAS Catalouge; https://www.ebi.ac.uk/gwas/). For each gene reported in the GWAS for a given disease, GeneCards dataset provides a relevance score based on the reported literature linking the gene to the disease (colored dots in Fig. 5A) while statistical evidence of their causal relationship to the risk of developing a disease is guaranteed by the GWAS data. The genes associated with neurological diseases (via GWAS) were not spread evenly across the gex-centrality and neurogenesis distributions (Fig. 5B) and they showed a significant enrichment at the percentile tails (see black arrows in Fig. 5C), supporting our hypothesis. Notably, this observation was typified by genes with a well-known role, such as: *APOE*, *TREM2* and *SORL1* (AD); *SCN1A, CUX2, PCDH7* and *CPLX1* (epilepsy); *SNCA, GBA* and *MAPT* (PD); or *MEF2C* and *CACNA1C* (ASD).

Discussion

In this work, we use the earliest time of neurogenesis (FirsT) reported for brain circuits to study adult brain networks that were reconstructed from structural-functional (resting-state) MRI. By correlating centrality metrics of complex networks with the FirsT, we observed a decreasing gradient of structural hubness in MACs and ROIs from those circuits generated earliest to those that appear later. This observation confirms our main working hypothesis that older nodes get richer in terms of hubness within brain networks. In the functional domain, the centrality of both ROIs and MACs follow opposite trends when compared to the structural case, so in general brain regions that developed later have a higher centrality.

Our results are consistent with brain differences early and late in development. The neurons generated earlier in the human brain mature in an environment favorable to cell growth, migration and axonal pathfinding. By contrast, neurons born later differentiate into a stiffer neuropil that has a dense extracellular matrix and thus, their growth and axonal pathfinding is more severely restricted by prior developmental maturation[21]. In addition, the growth of the brain itself plays a significant role in the formation of long-range connectivity. Whereas after four of weeks of gestation (GW) when the LC neurons begin their genesis, the brain measures 3-5 mm in length, whereas at eight GW when many cortical neurons are generated, the human fetal brain measures 27-31 mm[22]. Thus, the formation of general structural connectivity is affected by the timing of neurogenesis.

https://doi.org/10.1038/s41467-025-67785-3

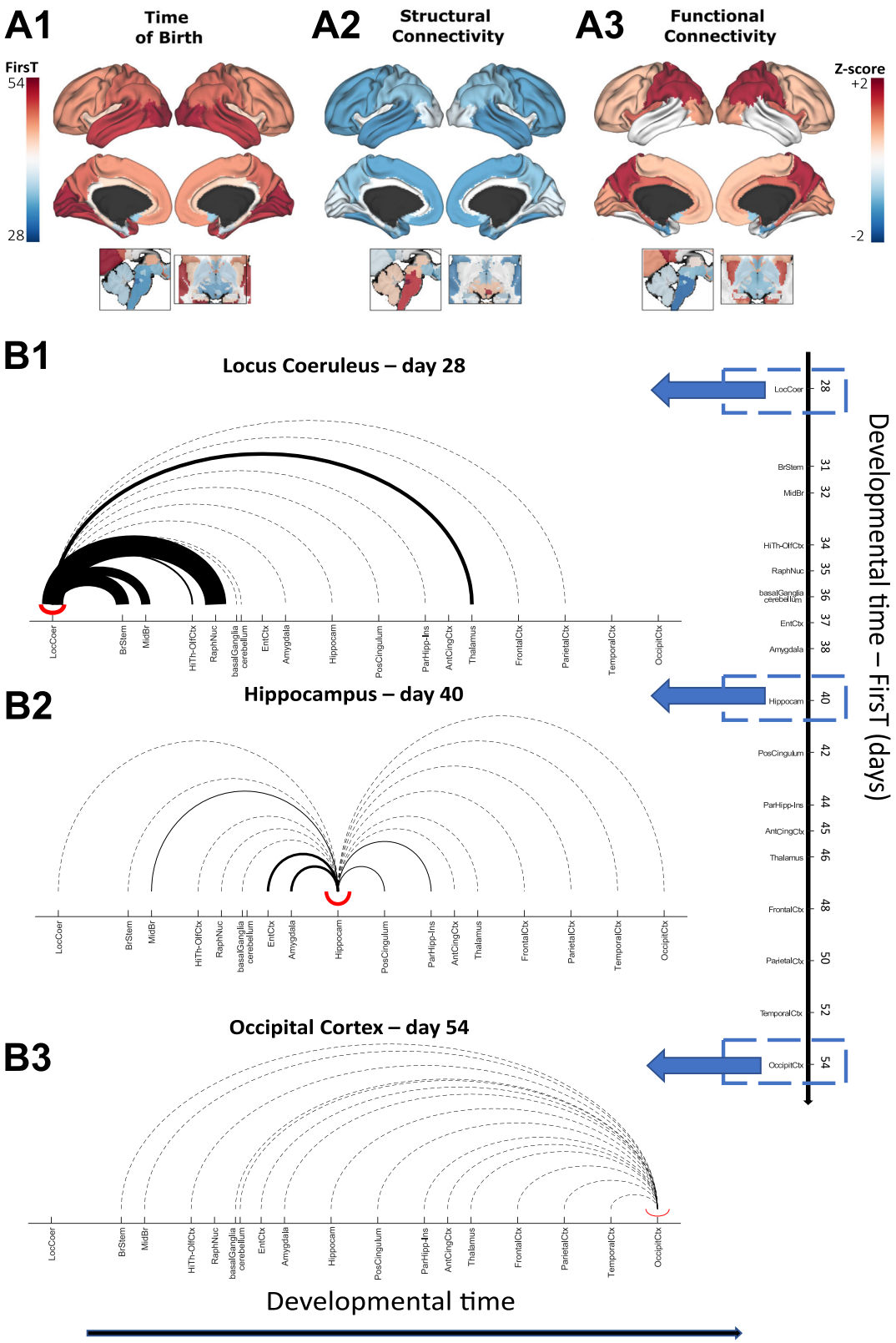

Fig. 3 | Visualization of brain connectivity and the first neurogenic birthdate. **A** The color coded glass brain maps of the eighteen MACs represents the FirsT (A1; see color bar on the left) and the z-score (see color bar on the right) of the eigenvector centrality for the SC (A2) and the FC (A3). **B** Linear temporal representation with arches of the MACs structural connectivity for the earliest (B1) generated MAC (Locus Coeruleus, FirsT 28), for a representative mid-term (B2) generated MAC (Hippocampus, FirsT 40) and for the latest (B3) generated MAC (Occipital Cortex, FirsT 54). The x-axis represents the developmental time of several FirsT, where the different MACs are located according to their FirsT. Note that the Basal Ganglia and Cerebellum overlap since their neurogenesis is initiated on day 36. The thickness of top black arches is proportional to the link weight between the MACs extracted from the 18 node adjacency matrix. Broken black lines mark the presence of connections but with little weight (i.e., below the lowest threshold for the visualization of solid lines). MATLAB (MathWorks, Inc.) was used for the computational analysis and plotting shown in this figure. Source data are provided as a Source Data file.

The older gets richer rule stems from the literature on the connectomics of birth-dated populations, both for neuronal populations that we were able to trace through MRI as well as for other smaller regions of the brain that cannot be distinguished at MRI resolution. In the former case, the neurons appearing first in the brain are those of the LC[23–26] and the brainstem and midbrain motor neurons, including those of the trigeminal mesencephalic nucleus[27]. These organize into small nuclei and although most of them cannot be segmented by MRI (here we only considered the LC and Raphe nuclei), our model predicts that they all are potentially relevant in terms of their connectivity. Noradrenergic LC neurons establish connections that span the whole brain[28], and both LC and trigeminal nuclei contribute to pathologies, such as AD when they degenerate[29–31].

Beyond the brainstem, pioneering studies on GABAergic hub cells[10] in the developing mouse hippocampus have shown how early born GABAergic neurons operationally and morphologically represent hub cells[11,32], also later identified in other structures[33] and in the adult mouse hippocampus[12]. Within the neocortex, where different neuronal populations are generated over sequential neurogenic stages[14] but where these birth-dated circuits cannot be tracked by MRI, hubs are related to neurogenesis. A recent computational study of neocortical circuits reported that targeted injury to layer 5 hub neurons produced the greatest damage to the structural-functional integrity of neocortical circuits[34]. Significantly, these layer 5 neurons are amongst the earliest neurons to be generated in the neocortex. Neuronal types generated earlier in the hippocampus, cortex, brainstem and mesencephalon might also adopt a hub role due to the timing of their neurogenesis. For example, stimulation of Purkinje cells in the cerebellum (an early born GABAergic neuronal type in a circuit that develops early) has been shown to inhibit spontaneous hippocampal seizures in a mouse model of temporal lobe epilepsy[35].

In terms of the topology of brain networks, we observe a decreasing gradient in the probability and strength of connections as a function of the difference in time of neurogenesis, both in structural and functional networks in the high and low degree of spatial resolution. Therefore, nodes generated at similar times showed a higher probability and strength of connection. This latter observation supports the hypothesis that brain networks follow a preferential age attachment rule, whereby nodes are more likely to connect if the time of their neurogenesis differs little. From a biological point of view, this might explain why neurons establish their main connections in a short temporal window of plasticity, named the critical period[36,37], before becoming functional and maturing. Therefore, neurons with an equivalent birthdate tend to share these permissive temporal windows, which allows their mutual/reciprocal connection. In this context, a recent study has shown in the hippocampal network that sequential neurogenesis affects connectivity and coactivity of neurons so that same birthdate neurons joined into cell assemblies[38].

In support of what we described in our research, computational models of structural brain network development demonstrate that connectivity patterns can arise from simple growth rules grounded in developmental timing, spatial embedding, and wiring cost minimization. For example, in ref. 39 it was shown that earlier-born nodes—particularly those centrally located—tend to become hubs due to their temporal and spatial advantage during network formation. These mechanisms account for key topological features of structural networks, including modularity and the presence of rich-club hubs.

Importantly, in addition to these computational insights, empirical studies have demonstrated a similar relationship between developmental timing and network topology in non-human species. Specifically, a strong correlation has been observed between the architectonic type of cortical areas and their number of connections in both the cat[40] and the macaque[41]. In these species, areas of lower architectonic type—those that tend to develop earlier—exhibit significantly more connections than later-developing, higher-type areas. These findings align with the so-called Architectonic Type Principle[42] and support the broader framework of the Structural Model of Connections originally formulated in ref. 43. Our current results suggest that this principle may generalize to the human brain, reinforcing the notion that developmental timing plays a universal role in shaping cortical connectivity—an idea also supported by studies in C. elegans and in simulated growth models[44].

While both structural and functional networks show preferential connectivity among similarly aged neurons, their formation rules may differ[45]. Structural networks are more influenced by spatial constraints and wiring cost minimization, which promote hub formation in early-born, centrally located nodes. In contrast, functional networks—shaped by dynamic, activity-dependent interactions—may be less constrained by physical distance, reflecting transient or polysynaptic coordination. These differences likely contribute to the varying strength of neurogenesis-related gradients observed across network types.

The rules of preferential age attachment and older gets richer extrapolate to the context of brain networks, which will therefore adhere to the pioneering model of Barabasi-Albert on the construction of scale-free networks and the genesis of network hubs.

Brain connectivity, like other biological features, is ruled and limited by natural selection. Due to the intimate relationship between development and evolution, it is likely that the rules that relate neurogenic birth to connectivity are conserved across species. Indeed, previous studies on the development of brain networks in *C. elegans* highlight the early evolutionary appearance of neuronal hubs[44]. Moreover, neurons linked by long-range connections tend to be generated at around the same neurogenic time and early in development[44], reinforcing the concept of a temporal windows of plasticity around neuronal birthdates. Ultimately, all connections are shaped evolutionarily to optimize axon length and the speed of connections[46,47], and other vertebrate brains are likely governed by the same rules of development and connectivity.

Indeed, the brain regions shown here to have the most hubness are highly conserved in the vertebrate brain[48], suggesting their crucial importance in all vertebrates. These regions include the posterior regions of the brain, such as the brainstem and mesencephalon, and the cerebellum, which are known to be relatively similar across the vertebrate taxa[49]. In part, the rule of the older gets richer suggests that ancient circuits -such as those in brainstem that are related to autonomic animal functions and directly involved in the animal's survival- are more influential in the network and more stable across evolution. For example, the highly conserved neurogenic formation of the cerebellum was recently demonstrated in several vertebrate species[50] and its remarkable orchestrating hub role has an impact on epileptic brain dynamics[35]. At the other end of the spectrum, circuits related to associative tasks, more strongly linked to cognition and human-specific behavior, are not necessarily conserved and they appear later in neurogenesis. We show here how their structural hubness (low) is inversely related to their functional one (high).

In relation to brain transcriptomics, we studied how spatial maps of gene expression in adult brains correlate with FirsT and structural-functional centrality maps. We found that genes whose expression is positively correlated with the centrality of structural circuits tend to show stronger expression in the circuits generated first. By contrast, genes whose expression is anti-correlated with the centrality of structural circuits show stronger expression in circuits in which neurogenesis occurs later. The opposite was observed for functional networks. Thus, the anti-correlation between gene expression in functional and structural connectivity shows that the transcriptomics of structural and functional networks appears to be differentially driven by genes whose expression is developmentally regulated. This is in agreement with the opposite trends we observed for functional and

https://doi.org/10.1038/s41467-025-67785-3

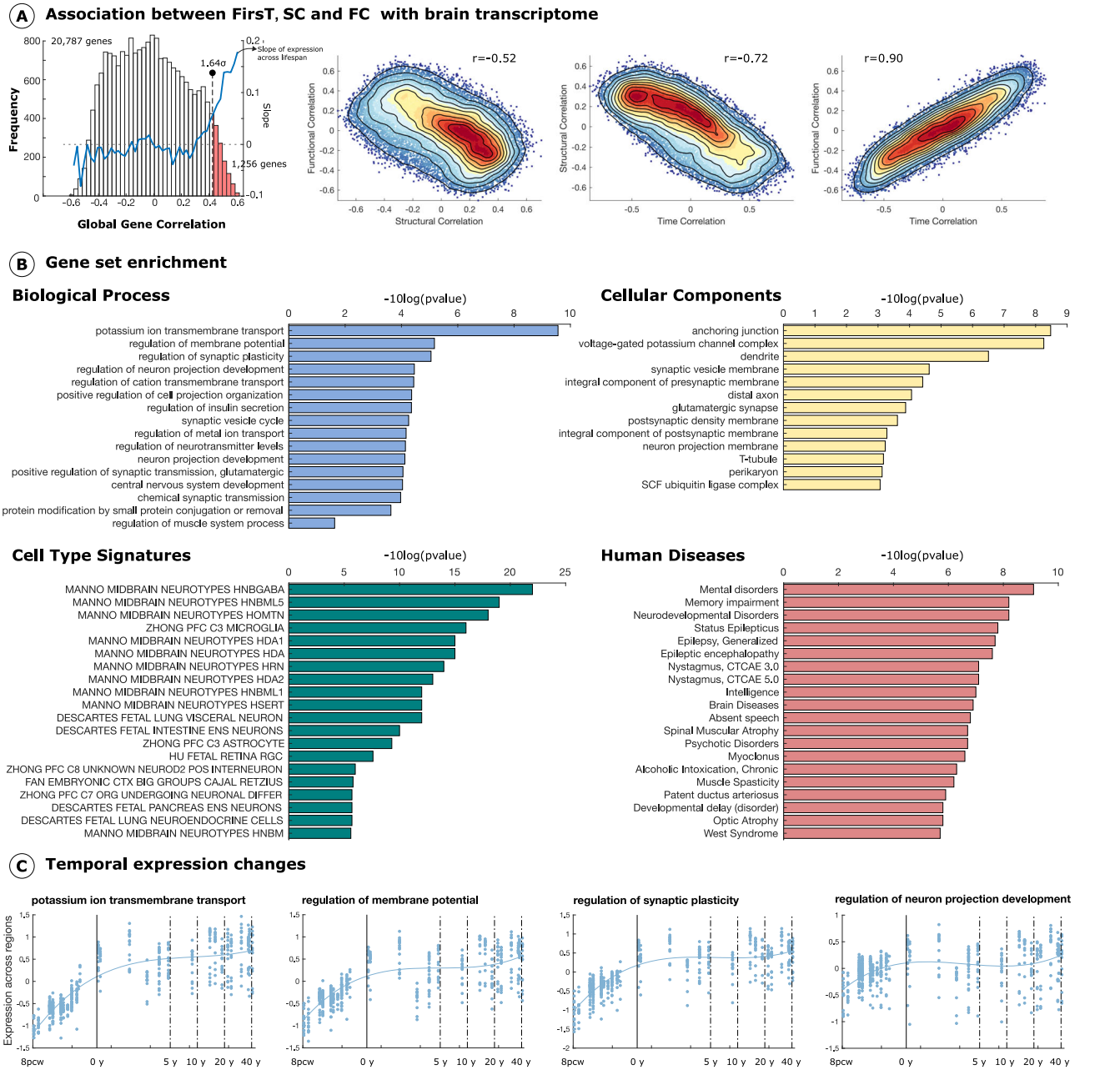

Fig. 4 | Transcriptome of brain circuits according to embryogenic age. A The distribution of the global gene correlation between the expression of 20,737 protein-coding genes from AHBA and the brain maps of FirsT, structural and functional eigenvector centrality is displayed. Blue line represents the mean slope computed between developmental time and the genes in each bin in BrainSpan transcriptomic atlas. Structural and functional centrality of the 2566 brain regions were downsampled to 90 region (to match gene expression space) and for each of the 90 regions one of the 18 FirsT was assigned. The scatter plots represent how comparable the values obtained when looking to the similarity between gene spatial expression and each modality are: genes similarity with functional correlation vs genes similarity with structural correlation; genes similarity with structural correlation vs genes similarity with FirsT; and genes similarity with functional correlation vs genes similarity with FirsT. **B** 1256 genes from the positive tail (6% of protein coding genes) – genes whose spatial expression is most similar to FirsT and functional and structural centrality – were used to compute gene set enrichment overrepresentation analysis (Fisher's Exact Test) for different annotations: biological processes, cell components, cell types, and human diseases. Monte Carlo simulation was used to generate random brain maps with similar autocorrelation as the original brain maps and assess if the significance of the annotations was biased for spatial autocorrelation. Only terms surviving multiple comparisons are reported; FDR $q < 0.05$. **C** The BrainSpan Atlas of the Developing Human Brain was used to represent the mean expression of the 4 top biological process across lifespan. Each dot represents a sample (a specific region of a particular donor). X-axis is time spanning from post conception weeks (pcw) to years (y). MATLAB (MathWorks, Inc.) was used for the computational analysis and plotting shown in this figure. Allen Human Brain Atlas data was utilized for the gene expression analysis shown in this figure[83]. Source data are provided as a Source Data file.

structural centrality as function of development. Previous studies into the genetic basis of human brain network structure and function presented converging evidence that anatomical connectivity is more strongly shaped by genetics than functional connectivity (see ref. 51 for a review). Here, we add that the developmental sequence (specifically the first time point of neurogenesis) is an additional key variable to interpret the genetic influence on the connectome, providing a key feature linking embryogenesis to the topology of adult brain networks. It also sheds light on the longitudinal reconstruction of developing brain networks, a phenomenon that presents key technical challenges[5].

https://doi.org/10.1038/s41467-025-67785-3

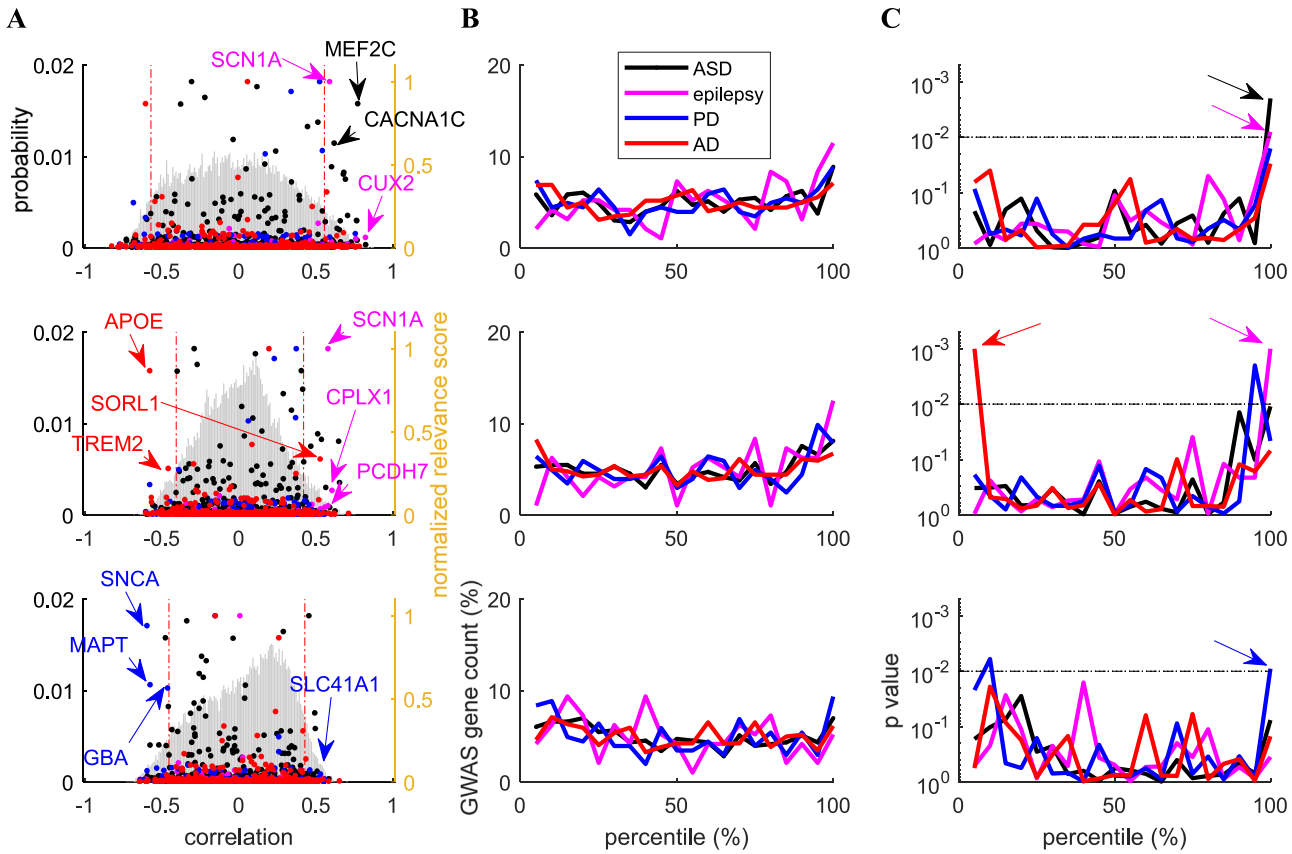

Fig. 5 | Correlations between the maps of the gene transcriptome, neurogenesis and hubness in relation to Autism Spectrum Disorder, epilepsy, Parkinson's and Alzheimer's disease. For each gene the spatial expression in the brain was correlated to the spatial maps of eigenvector centrality and neurogenesis (note that from the sub-sampled brain transcriptomes, 90 brain regions were considered: see Methods). **A** Probability distribution of the correlations (light gray histogram, left axis) between transcriptomics (20,787 genes) and neurogenesis (top plot), functional centrality (middle plot) and structural centrality (bottom plot). The normalized relevance score of the GWAS genes listed for each disease (obtained from the GeneCards databases; Note that normalization is computed separately for each disease; see Methods) has been plotted with dots (right axis). The colors used to display the results for the different diseases in panel A-C, are shown in the inset legend of the top plot of panel B. Vertical broken lines highlight the lowest and top five percentile interval. Colored labels and arrows mark the most relevant representative GWAS genes with correlations in the highlighted extreme percentiles. **B** For each disease, the normalized count (percentage of gene per interval) of GWAS genes in five percentile intervals of the correlation distribution (light gray histogram of panel A) is plotted for the different diseases (legend of colors is in the inset of the top plot)). **C** The *P*-value of the two-side non-parametric permutation test is displayed quantifying whether the number of GWAS-associated genes in each correlation bin is significantly higher than expected by chance. The null model for the test was calculated from one thousand reshuffled replications designed to account for spatial dependencies of both the centrality maps and gene-expression data. The broken horizontal black line represents the significance threshold of $P < 0.01$. MATLAB (MathWorks, Inc.) was used for the computational analysis and plotting shown in this figure. Allen Human Brain Atlas data was utilized for the gene expression analysis shown in this figure[83]. Source data are provided as a Source Data file.

Since enrichment analysis in relation to human diseases suggested a role in mental and neurological disorders, next we explored if genes with a known role in neurological diseases are linked closely to network centrality and neurogenesis with the potential to exert an influence on key network hubs.

Interestingly, in a recent similar study on the UK Biobank database focused on the genetic architecture (heritability) underlying the white matter connectome (i.e. solely focused on structural connectivity)[52], enrichment analyses highlighted the key role of neurodevelopmental processes including neurogenesis, neural differentiation, neural migration, neural projection guidance, and axon development. In addition, structural connectivity displayed significant associations also to polygenic scores for psychiatric, neurological, and behavioral traits.

In our research, we studied the correlation between FirsT, structural and functional network centrality maps, and the expression of genes associated with epilepsy, Autistic Spectrum Disorder (ASD), PD, and AD, models of neurodevelopmental and neurodegenerative diseases. First, we observed that a significant number of genes linked to ASD and epilepsy show high positive correlations to neurogenesis and functional centrality maps in agreement with the evidence that ASD and several forms of epilepsy (such as Dravet syndrome and infant epilepsy) is linked to late brain developmental processes[53] and supporting the idea that ASD and infant genetic forms of developmental epilepsy can lead to functional brain maps' lesion rather than structural ones[54]. Distinctly, in our model a significant population of genes related to PD express similarly to structural centrality maps, so highly expressed in early generated structures (i.e., structural brain hubs) and with lower expression in later developed structures. This support the idea that PD is a disease linked to targeted structural lesions, such as those ones occurring in the dopaminergic neuronal population in the basal midbrain (which is the third in the rank of neurogenesis). In the case of the AD, we identified a significant high number of genes with anti-correlated expression to functional centrality, so potentially poorly expressed in functional hubs (late structures) and viceversa. Therefore, we conclude that dysfunctional properties of the proteins coded by these genes, maybe also associated to alterations in their expression levels, can have potential high impact in brain hubs at

developmental, functional and structural levels and can play a key role in the etiology and associated dysfunctions of brain pathologies. Highlighting some well-known genes with top correlation ranks (see supplementary auxiliary tables) in relation to the studied brain pathologies, we found a contribution of four genes known to drive PD: *SNCA*[55,56] that encodes the parkinsonism-associated Lewy body protein alpha synuclein, *MAPT*[57] encoding the microtubule-associated protein tau, GBA[58] encoding the lysosomal enzyme glucocerebrosidase and *SLC41A1*[59] encoding a magnesium transporter (a candidate for the causative gene in the *PARK16*). Together our results indicate that *SNCA*, *MAPT* and *GBA* are expressed more weakly in nodes with higher structural centrality under physiological conditions and viceversa for *SLC41A1* (Fig. 5A). We also found associations for the gene encoding apolipoprotein E, *APOE*, which is directly related to AD, cerebral amyloid angiopathy, PD and other neurological diseases[60], and for *TREM2*, a receptor expressed in myeloid cells 2 that is related to microglial biology, a high risk of developing AD[61] and prion diseases[62]. In addition, the *SORL1* gene that encodes the sortilin-related receptor, and that has been associated with early and late-onset AD[63], was also found to have a strong positive correlation with functional centrality. In the case of ASD, we highlight the gene *MEF2C*[64] which regulates cortical inhibitory and excitatory synaptic balance and *CACNA1C* coding for a calcium channel linked to selective autophagy and altered axon targeting and behavior[65]. For epilepsy, we highlight the presence of the *SCN1A* gene, which encodes the Alpha 1 Subunit of the Sodium Voltage-Activated Channel, occupying position 144 in correlation with the functional centrality of 20,787 genes considered, and with a known causal relationship to Dravet Syndrome, a rare genetic disease causing one of the most devastating forms of childhood generalized epilepsy[66]. In this context, when looking at the transcriptomics' targets underlying last approved drug for Dravet Syndrome, specifically Fenfluramine[67] that is an agonist of the serotonin 5-$HT_{2A/B/C}$ receptors, we observe that the expression of *5-HT$_{2A}$* is highly correlated to FirsT (correlation 0.75 ranking 76 out of 20787 genes) and both *5-HT$_{2A}$* and *5-HT$_{2C}$* are in the extreme percentiles of functional centrality distribution (respectively with correlation of 0.43 and −0.48 lying in the 95.3 percentile and 2.1 percentile of the functional centrality distribution). Overall, this shows that our model can capture not only key transcriptomic regulator for the onset of epilepsy, but also for its treatment. Future investigations will highlight possible similar results and conclusions in relation to other neurological diseases.

Notably, many genes known to underlie neurodevelopmental disorders (as the ones for example highlighted in ref. 68) lie in the extreme percentiles of the FirsT or centrality distributions (such as *CACNA1A*, *DEPDC5*, *SCN8A*, and more).

As a result of both human disease enrichment and deeper analyses of four neurological conditions, our results provide support for the hypothesis that neurological diseases may be linked to key topological alterations to brain networks in relation to node hubness[69]. Thus, altered transcription of genes whose expression correlates closely with network centrality could lead to profound neurological lesions and disease. In this context, stroke and other circuit damage to early-generated brain structures (such as those in the brainstem region) are known to have life-threatening consequences relative to later-generated cortical damage[70].

Methods

Neurogenesis timeline of brain circuits – Selection of circuits

To select the circuits to study, we needed to reach a compromise between the conflicting resolution of MRI and the developmental structural units. Certainly, there are hundreds of brain structures and circuits that can be segmented by MRI (cf. the list of areas that were identified in the AAL classification[71] and others[72]), although many of these regions do not develop independently (for example, the many neocortical areas). By contrast, there are brain regions that are developmentally relevant but that cannot be precisely segmented by MRI (e.g., thalamic nuclei). Therefore, the two criteria followed to select the list of brain circuits that ultimately studied were developmental independence and MRI segmentability.

Developmental independence: Based on how the brain is generated during embryonic development, we chose brain regions that were derived from independent units of the early differentiated brain, called fundamental morphogenic units (FMUs[73]). Early in development, all vertebrate brains divide into different vesicles: secondary prosencephalon, diencephalon, midbrain, and hindbrain. Each of these vesicles can be segmented into several neuromeres, which are developmentally independent rings of the neural tube destined to form the major brain regions. Each neuromere contains several FMUs along its dorsal-ventral axis (Fig. 1A) and the neurons within a given FMU are formed mostly by neurogenesis. For example, the m1 neuromere in the mesencephalon gives rise to most of the neurons in the superior colliculus, so we consider the superior colliculus to be a developmental unit. When a FMU generates through development several brain regions that we can resolve through MRI (e.g., the occipital neocortex), we have merged these structures into a single MAC, as those regions are not developmentally independent and their FirsTs are therefore the same. The literature available shows the specific date of birth of the different populations in each developmental unit in several mammalian species (see below).

MRI segmentability: The human brain evolved following an unprecedented expansion of the neocortex, which develops from a single developmental unit[74]. But this expansion came at the expense of shrinking many brain regions, such that some are so small that they cannot be segmented at MRI resolution. For example, the brainstem and pons are generated from the rhombencephalon, and there are up to 11 rhombomeres, each of which hosts a number of FMUs but none of which can be segmented by MRI. Thus, we identified consistently segmentable brain structures from MRIs. Consequently, no circuit was assigned to two different birth dates. Most brain structures were generated during a neurogenic period but the first neurogenic time (FirsT) was considered to be the first day after which neurons began to appear.

Neurogenesis timeline of brain circuits - Estimation of FirsT

We hypothesize that the strength of adult connectivity in a given region depends on the developmental stage at which it forms.[75]. The same method to estimate human FirsT was applied for all circuits, this is a summary of the pipeline:

1.Experimental birthdating of the neurons of a given brain area through DNA-synthesis labeling (via BrdU or ^{3}H-Thymidine administration) in non-human species (references in Table 1).

2.Determination of the developmental stage at which the first neurons of that brain region were generated in that species (stages on Table 1).

3.Translation of this non-human stage into human developmental stage via translatingtime.org[75] which provides the FirsT value of the given brain region. This is possible and reliable thanks to the great conservation of the developmental sequence found across mammals[75].

Each FirsT data point is based on at least one article, all articles are referenced in Table 1. When several independent articles displayed research on the same structure (i.e., the locus coeruleus), these led to the same FirsT measurement. Therefore, our FirsT data points represent a single embryonic day as FirsT, not a range/interval.

No single database contains birthdate information for all brain regions examined.

MRI DATASET AND PROCESSING

Participants. Neuroimaging data was acquired from the Human Connectome Project (WU-Minn Consortium - PIs David Van Essen and Kamil Ugurbil: 1U54MH091657), funded by the 16 National Institutes of

Health (NIH) that support the NIH Blueprint for Neuroscience Research and by the McDonnell Center for Systems Neuroscience (Washington University). For this study, we took data from $N = 184$ healthy subjects acquired at 7 Tesla (72 males, 112 females; 24 participants between 22–25 years, 84 between 26–30 years, 73 between 31–35 and 2 over 36). High-resolution structural T1 images, functional magnetic resonance images at rest (fMRI) and diffusion tensor images (DTI) were used (for more information on the acquisition parameters see Supplementary Methods and the Human Connectome Project documentation - http://www.humanconnectome.org/).

Image preprocessing

Minimal pre-processed data was downloaded from the Human Connectome[76]. T1 structural images were aligned to the anterior and posterior commissures, skull stripped, corrected for gradient distortion and bias fields, and the non-linear transformation to the MNI152 standard space was computed. Using a one-step resampling approach, resting state functional data was corrected for gradient-nonlinearity-induced distortion and movement within runs using a rigid body transformation (six parameter linear transformation) and EPI distortion. Both the transformation from the reference image to the structural T1 image, and from T1 to the standard space were also performed through a one-step resampling approach. A subject specific functional data projection to MNI152 was obtained. Diffusion images were normalized for b0 intensity and EPI distortion, movement and eddy currents were corrected, as were gradient non-linearities. The B0 image was co-registered to the subject's anatomical T1 images. For more details on the minimal pre-processing of the human connectome refer to the original paper[76]. To further reduce the noise in the functional data, a general linear model was used to remove linear and quadratic trends, as well as the contribution of movement, the cerebrospinal fluid and white matter signals. Additionally, band-pass filtering (0.01–0.08 Hz) and spatial smoothing with an isotropic Gaussian kernel of 6 mm FWHM was applied.

Brain parcellation in macrocircuits (MACs) and regions of interest (ROIs)

Several regions from different brain MRI atlases were combined to generate 18 different macrocircuits. The atlases used included the Automated Anatomical Labeling (AAL[71]), Freesurfers Desikan-killiany atlas[77], CIT168 subcortical atlas[78] and locus coeruleus atlas[79]. The LC and raphe nuclei were chosen as the functional ROIs that englobed them (for further details see Table 1).

Brain parcellation was performed after clustering the functional data to study network properties with about 2500 ROIs. In particular (and similar to ref. 15), clustering was performed based on temporal correlations between pairwise voxel time series that impose a constraint to ensure spatially contiguous ROIs. This was performed in two stages: 1. clustering at the single subject level; and 2. a second clustering applied to individual subject data. To avoid ROIs with voxels belonging to several circuits rather than performing clustering on the whole brain, this strategy was applied separately for each macrocircuit. Small circuits were neglected and those voxels were inserted into the nearest circuit. After parcellation, we took all ROIs overlapping some of the existing circuits, resulting in 2566 regions covering the whole brain.

STRUCTURAL AND FUNCTIONAL BRAIN NETWORKS

After image processing, the connectivity matrices were obtained representing two modalities composed of 2566 ROIs: structural and functional networks. Individual subject functional connectivity matrices were obtained by averaging all the time series of the voxels belonging to each ROI generated, and by calculating the Pearson correlation value between the time series corresponding to each pair of ROIs. The average of the functional matrices across all subjects was then calculated. Only positive links with an average minimal correlation of 0.19 were considered. This value corresponds to a p-value of 0.7×10^{-9} when calculated on time series composed by 900 points. Such p-value threshold was chosen in order to apply a strict Bonferroni correction on a 0.01 p-value of multiple comparisons, i.e., divided by the number of links in the adjacency matrix (which correspond to half of the elements in matrix excluding the diagonal considering that adjacency matrices are symmetric by definition in our methodology, i.e., (2566*2566)−2566/2). This final matrix defined the average functional connectivity matrix: FC, and it had a connectivity density of 6.5%.

FSL functions were used to quantify the individual subject structural connectivity matrices. First FSL BEDPOSTX was used to model crossing fibers and subsequently, probabilistic tractography was performed with PROBTRACKX to generate a #ROI × #ROI matrix per subject. Matrices were normalized between 0 and 1 dividing each element by their maximum. The average across subject matrices were finally obtained and only the top 5% of higher weights were considered to create the structural connectivity matrix, SC, consistent with previous studies[18]. ROIs' hubness quantified with EC in the SC in the dense (when all links were considered) or sparse (when only top 5% links were considered) adjacency matrix, correlated with a 0.99 value ($p < 10^{-10}$) so they did not show significant differences. For both the functional and structural matrices, the principal diagonal elements were set to zero to avoid ROI self-connectivity interactions. Note that following the above-described procedures of thresholding of structural and functional matrices, the overall network analysis presented in this MS were carried out on adjacency matrices with similar level of network connectivity density of 5% and 6.5%, respectively in the structural and functional levels.

COMPLEX NETWORKS ANALYSIS

Through their construction, all the networks analyzed were symmetric and weighted, with non-negative values.

Being centrality measures very highly correlated in most networks including the brain[80] we chose EC as reference centrality metric in our study being the one showing less variability both when considering all link weights or when applying thresholds to structural or functional adjacency matrices. EC was calculated using MATLAB (Mathworks) function from the Brain Connectivity Toolbox (https://sites.google.com/site/bctnet/measures/list). When we dissected the global connectivity of the MACs through the links of their englobed ROIs (Fig. 2B, Supplementary Fig. 3 and 4), we also calculated an 18 x 2566 connectivity matrix (GC) where each row represents the average weights of the links connecting the ROIs within the MAC to the rest of the brain ROIs according to:

$$GC_{\alpha j} = \frac{1}{|M_\alpha|} \sum_{i \in M_\alpha} C_{ij} \quad (1)$$

where M_α is the set of ROIs englobed in the MAC α, $|M_\alpha|$ is the cardinality of the set M_α, $1 <= \alpha <= 18$ and i are the indexes of the ROIs belonging to the MAC α.

The global MAC strength (G-st, Fig. 2B) of the MAC α was calculated as the average of elements $GC_{\alpha j}$, where $1 <= j <= 2566$. The global link weight (G-w, Supplementary Fig. 3 and 4) between two MACs α and β was calculated as the average of the elements $GC_{\alpha z}$ where z is the set of ROIs belonging to the MAC β.

To remove the potential bias introduced by the differential presence of white or gray matter in the ROIs, each individual partial volume of white and gray matter was estimated using the FSL FAST tool[81]. For each functional ROI the average white and gray matter partial volume estimates were computed from the group average. We used a Spearman partial correlation to calculate the correlation

between structural (functional) centrality and FirsT, while regressing out white (gray) matter partial volume estimates per ROI or per MAC (considering the average across the ROIs within each MAC).

The difference in neurogenesis time (see Fig. 2C) between two ROIs (ΔFirsT) was defined as:

$$\triangle FirsT_{ab} = \left| FirsT_a - FirsT_b \right| \quad (2)$$

where (a,b) is a pair of ROIs.

If F is the set of elements in the matrix satisfying the condition ΔFirsT=D (i.e. all possible links with ΔFirsT=D; 0 < = D < =max(ΔFirsT) = 26 days), the probability of a structural (functional) connection with ΔFirsT=D was calculated as the fraction of existing links in the adjacency matrix SC (FC) out of F. Similarly, for the same ΔFirsT=D and set F, the average link weight was calculated over the existing links of the adjacency matrix SC (FC).

To ensure that correlations between EC maps and the different variables were not due to spatial dependencies in neuroimage maps we used a Monte Carlo simulation test. First, we computed the spatial autocorrelation of the neuroimage maps and generated 1000 random maps with the same spatial autocorrelation using BrainSMASH[82]. Then the correlations were repeated with the 1000 random maps and a p-value of the likelihood of the obtained correlation was computed by counting how many times a random map with similar spatial autocorrelation gives a correlation higher than the one obtained in the original map.

GENETIC FINGERPRINT OF BIRTHDATE CIRCUITS

To investigate the genetic fingerprints of the circuits' birthdays, we used the transcriptome dataset from the AHBA[83]. The AHBA provides whole-brain genome-wide expression values for 20,737 protein encoding genes extracted from 3702 brain samples and distributed spatially over six human post-mortem brains. Using the brain sample information, brain maps representing the spatial distribution of each gene in the 18 circuits was generated based on recent recommendations[84]: i) expression values from multiple probes were averaged; ii) each sample was mapped to one of the 18 circuit atlases, with samples falling outside mapped to the nearest circuit if this was closer than 3 mm; iii) for each individual the median expression values were calculated across all samples that mapped to the same circuit; iv) a z-score was used for inter-individual normalization of gene expressions; v) a group expression map was computed by calculating the mean expression values of the six individual donors. While AHBA dataset has not enough spatial coverage for the computation of genetic expression values at each of the 2566 regions, we generated a 90 regions parcellation to gain more detailed expression maps compared to the 18 regions. The expression atlas containing 90 brain regions was based on the 68 cortical regions of the Desikan-Killiany atlas, the 16 subcortical regions from freesurfer, the cerebellum, brainstem, LC and the dorsal raphe nucleus (see Supplementary Fig. 5). This 90 regions' atlas was used to assess the genetic associations of the structural and functional organization of the brain. The EC of the 2566 values falling into each 90 regions was averaged to transform 2566 functional and structural centrality maps to 90 regions.

To search the underlying genetic fingerprints of both the microcircuit FirsT, and the brain functional and structural centrality (Fig. 4A, B), a global gene correlation (GGC)for each of the 20,737 protein-coding genes was computed.

$$r(g) = \frac{r_{FirsT,90}(g) - r_{SCC,90}(g) + r_{FCC,90}(g)}{3} \quad (3)$$

The score r for a given gene g is the average Spearman correlation between the expression of gene g with the FirsT projected to 90 regions $r_{FirsT,90}(g)$, with structural connectivity centrality in 90 regions $r_{SCC,90}(g)$ and with functional connectivity centrality in 90 regions $r_{FCC,90}(g)$. The sign of the Spearman correlation of structural connectivity was inverted as it follows an inverse pattern relative to the FirsT and functional connectivity. Genes with a score >1.64 standard deviations from the distribution obtained were used for further analyses (r > 0.43; 1256 genes).

An overrepresentation analysis was used to find common functional annotations in the obtained gene list. Same approach was used when performing the enrichment of FirsT, where instead using the total r score only the $r_{FirsT,90}(g)$ is used (Supplementary Fig. 6). Gene set enrichment was computed using Metascape[85] (http://www.metascape.org/) for biological processes and cell component annotations from Gene Ontology, human diseases annotations from DisGeNET[86], and cell type signatures[85]. Only terms surviving to multiple comparisons are reported; FDR q < 0.05. We used Monte Carlo simulation to assess significance of each of the obtained significant annotations, to overcome false-positives bias due to gene co-expression spatial autocorrelation[87]. Following the same approach as before, first, we used BrainSMASH[82] to generate 1000 surrogate maps with matching spatial autocorrelation with 90 regions FirsT, and structural and functional centrality maps. Then, for each surrogate map we computed the spatial similarity (Spearman correlation) with 20,737 protein coding genes and we used the list of genes with a similarity >1.64 standard deviations from the obtained distribution to perform an over-representation analysis. For each of the annotations we quantified how many times the enrichment value was higher in the original data compared to the surrogate maps and we generated a p-value of the significance. All the annotations that were not significant (FDR-corrected) were removed.

We also used The BrainSpan Atlas of the Developing Human Brain to further validate the association between found biological process with a developmental trajectory[20]. 492 samples are available from 35 individuals covering 16 cortical and subcortical brain regions from eight post conception weeks to 40 years. First a z-score was used for inter-individual/region normalization of gene expressions. Then for each gene a general linear model was used to fit a model with the association between the logarithm of development time (days post conception) and gene expression. The mean slope of all the genes in each bin of the AHBA association was computed and displayed in Fig. 4a, to show the association between the spatial expression of AHBA and temporal expression of BrainSpan atlas associated with development. Additionally, the genes associated with the top four biological processes of the previous analyses were mean averaged and a 3rd degree polynomial fit was used to plot the temporal trajectory along lifespan.

Regarding genetic and neurological diseases, our analysis was based on the full gene lists related to Epilepsy, ASD, PD and AD as reported by the Genome-Wide Association Study (GWAS) and downloaded from https://www.ebi.ac.uk/gwas/ (GWAS). For these lists of genes, we used the corresponding relevance score for each disease from Genecards database (www.genecards.org). Given a pathology, we normalized the relevance scores dividing by its maximum, in this way we could use a common index which could be plot across pathologies (see normalized relevance score in Fig. 5) For a detailed definition of the relevance score relative to the disease, see https://www.genecards.org/Guide/Search. The distribution of the genes from the GWAS Catalouge (Fig. 5) was analyzed in intervals of five percentiles. The enrichment for GWAS Catalouge genes in the outermost percentiles vs the rest of the distribution was tested using the previously generated thousand randomizations that preserved both spatial dependencies in the variable representing neurogenesis, functional or

structural centrality. In regard to gene expression dependency, the correlation in the expression of the genes in the brain parcellation was preserved in each random trial by reshuffling in the same order the values of the expression across the brain parcellation. Given one

thousand randomizations, p-values reported in Fig. 5C were calculated with a 0.001 resolution.

The lists of genes from the GWAS list in the outermost percentiles (see vertical black broken lines in Fig. 5A) are reported as Auxiliary Supplementary tables, with information on the structural and functional correlations (value, rank and percentile), and the relevance score (value, rank and percentile).

Reporting summary

Further information on research design is available in the Nature Portfolio Reporting Summary linked to this article.

Data availability

All neuroimaging data supporting this study's finding are available in the Human Connectome Project website https://db.humanconnectome.org/. The Allen Human Brain Atlas (AHBA) transcriptomic data is available at https://human.brain-map.org. Source data are provided with this paper. All non-publicly archived source data generated during this study are provided with this paper in the Source Data file. Source data are provided with this paper.

Code availability

All codes related to study analysis are available from the corresponding author (P.B.) upon request.

References

1. Betzel, R. F. & Bassett, D. S. Multi-scale brain networks. *NeuroImage* **160**, 73–83 (2017).
2. Buzsáki, G. *Rhythms of the Brain*. (Oxford University Press, 2006).
3. Fox, M. D. Mapping symptoms to brain networks with the human connectome. *N. Engl. J. Med.* **379**, 2237–2245 (2018).
4. Cisek, P. & Hayden, B. Y. Neuroscience needs evolution. *Philos. Trans. R. Soc. B* **377**, 20200518 (2022).
5. Oldham, S. & Fornito, A. The development of brain network hubs. *Develop. Cogn. Neurosci.* **36**, 100607 (2019).
6. Cimini, G. et al. The statistical physics of real-world networks. *Nat. Rev. Phys.* **1**, 58–71 (2019).
7. Broido, A. D. & Clauset, A. Scale-free networks are rare. *Nat. Commun.* **10**, 1017 (2019).
8. Bassett, D. S., Khambhati, A. N. & Grafton, S. T. Emerging frontiers of neuroengineering: a network science of brain connectivity. *Annu. Rev. Biomed. Eng.* **19**, 327–352 (2017).
9. Barabási, A.-L. & Albert, R. Emergence of scaling in random networks. *Science* **286**, 509–512 (1999).
10. Bonifazi, P. et al. GABAergic hub neurons orchestrate synchrony in developing hippocampal networks. *Science* **326**, 1419–1424 (2009).
11. Picardo, M. A. et al. Pioneer GABA cells comprise a subpopulation of hub neurons in the developing hippocampus. *Neuron* **71**, 695–709 (2011).
12. Bocchio, M. et al. Hippocampal hub neurons maintain distinct connectivity throughout their lifetime. *Nat. Commun.* **11**, 4559 (2020).
13. van den Heuvel, M. P. & Sporns, O. Network hubs in the human brain. *Trends Cogn. Sci.* **17**, 683–696 (2013).
14. Molnár, Z. et al. New insights into the development of the human cerebral cortex. *J. Anat.* **235**, 432–451 (2019).
15. Diez, I. et al. A novel brain partition highlights the modular skeleton shared by structure and function. *Sci. Rep.* **5**, 10532 (2015).
16. Diez, I. et al. Enhanced prefrontal functional–structural networks to support postural control deficits after traumatic brain injury in a pediatric population. *Netw. Neurosci.* **1**, 116–142 (2017).
17. Rasero, J. et al. Group-level progressive alterations in brain connectivity patterns revealed by diffusion-tensor brain networks across severity stages in Alzheimer's disease. *Front. Aging Neurosci.* **9**, 215 (2017).
18. Bonifazi, P. et al. Structure–function multi-scale connectomics reveals a major role of the fronto-striato-thalamic circuit in brain aging. *Hum. Brain Mapp.* **39**, 4663–4677 (2018).
19. He, C. et al. Structure–function connectomics reveals aberrant developmental trajectory occurring at preadolescence in the autistic brain. *Cereb. Cortex* **30**, 5028–5037 (2020).
20. Diez, I. & Sepulcre, J. Unveiling the neuroimaging-genetic intersections in the human brain. *Curr. Opin. Neurol.* **34**, 480–487 (2021).
21. Martínez, G. F. et al. Extracellular matrix stiffness negatively affects axon elongation, growth cone area and F-actin levels in a collagen type I 3D culture. *J. Tissue Eng. Regen. Med.* **16**, 151–162 (2022).
22. Stiles, J. & Jernigan, T. L. The basics of brain development. *Neuropsychol. Rev.* **20**, 327–348 (2010).
23. Altman, J. & Bayer, S. A. Development of the brain stem in the rat. I. Thymidine-radiographic study of the time of origin of neurons of the lower medulla. *J. Comp. Neurol.* **194**, 1–35 (1980).
24. Altman, J. & Bayer, S. A. Development of the brain stem in the rat. III. Thymidine-radiographic study of the time of origin of neurons of the vestibular and auditory nuclei of the upper medulla. *J. Comp. Neurol.* **194**, 877–904 (1980).
25. Altman, J. & Bayer, S. A. Development of the brain stem in the rat. V. Thymidine-radiographic study of the time of origin of neurons in the midbrain tegmentum. *J. Comp. Neurol.* **198**, 677–716 (1981).
26. Steindler, D. A. & Trosko, B. K. Two types of locus coeruleus neurons born on different embryonic days in the mouse. *Anat. Embryol.* **179**, 423–434 (1989).
27. Altman, J. & Bayer, S. A. Development of the brain Stem in the rat. II. Thymidine-radiographic study of the time of origin of neurons of the upper medulla, excluding the vestibular and auditory nuclei. *J. Comp. Neurol.* **194**, 37–56 (1980).
28. Kebschull, J. M. et al. High-throughput mapping of single-neuron projections by sequencing of barcoded RNA. *Neuron* **91**, 975–987 (2016).
29. Goto, T. et al. Neurodegeneration of trigeminal mesencephalic neurons by the tooth loss triggers the progression of Alzheimer's Disease in 3×Tg-AD model mice. *JAD* **76**, 1443–1459 (2020).
30. Beardmore, R., Hou, R., Darekar, A., Holmes, C. & Boche, D. The locus coeruleus in aging and Alzheimer's disease: a postmortem and brain imaging review. *JAD* **83**, 5–22 (2021).
31. Jacobs, H. I. L. et al. In vivo and neuropathology data support locus coeruleus integrity as indicator of Alzheimer's disease pathology and cognitive decline. *Sci. Transl. Med.* **13**, eabj2511 (2021).
32. Cossart, R. Operational hub cells: a morpho-physiologically diverse class of GABAergic neurons united by a common function. *Curr. Opin. Neurobiol.* **26**, 51–56 (2014).
33. Mòdol, L. et al. Spatial embryonic origin delineates GABAergic hub neurons driving network dynamics in the developing entorhinal cortex. *Cereb. Cortex* **27**, 4649–4661 (2017).
34. Gal, E. et al. The role of hub neurons in modulating cortical dynamics. *Front. Neural Circuits* **15**, 718270 (2021).
35. Krook-Magnuson, E., Szabo, G. G., Armstrong, C., Oijala, M. & Soltesz, I. Cerebellar directed optogenetic intervention inhibits spontaneous hippocampal seizures in a mouse model of temporal lobe epilepsy. *Eneuro* **1**, ENEURO.0005-14.2014 (2014).
36. Dehorter, N. & Del Pino, I. Shifting developmental trajectories during critical periods of brain formation. *Front. Cell. Neurosci.* **14**, 283 (2020).
37. Wong-Riley, M. T. T. The critical period: neurochemical and synaptic mechanisms shared by the visual cortex and the brain stem respiratory system. *Proc. R. Soc. B.* **288**, 20211025 (2021).
38. Huszár, R., Zhang, Y., Blockus, H. & Buzsáki, G. Preconfigured dynamics in the hippocampus are guided by embryonic birthdate and rate of neurogenesis. *Nat. Neurosci.* **25**, 1201–1212 (2022).

39. Kaiser, M. & Hilgetag, C. C. Development of multi-cluster cortical networks by time windows for spatial growth. *Neurocomputing* **70**, 1829–1832 (2007).
40. Beul, S. F., Grant, S. & Hilgetag, C. C. A predictive model of the cat cortical connectome based on cytoarchitecture and distance. *Brain Struct. Funct.* **220**, 3167–3184 (2015).
41. Beul, S. F., Barbas, H. & Hilgetag, C. C. A predictive structural model of the primate connectome. *Sci. Rep.* **7**, 43176 (2017).
42. Hilgetag, C. C., Beul, S. F., Van Albada, S. J. & Goulas, A. An architectonic type principle integrates macroscopic cortico-cortical connections with intrinsic cortical circuits of the primate brain. *Netw. Neurosci.* **3**, 905–923 (2019).
43. García-Cabezas, M. Á, Zikopoulos, B. & Barbas, H. The structural model: a theory linking connections, plasticity, pathology, development and evolution of the cerebral cortex. *Brain Struct. Funct.* **224**, 985–1008 (2019).
44. Varier, S. & Kaiser, M. Neural development features: spatio-temporal development of the caenorhabditis elegans neuronal network. *PLoS Comput. Biol.* **7**, e1001044 (2011).
45. Bullmore, E. & Sporns, O. The economy of brain network organization. *Nat. Rev. Neurosci.* **13**, 336–349 (2012).
46. Pavlovic, D. M., Vértes, P. E., Bullmore, E. T., Schafer, W. R. & Nichols, T. E. Stochastic blockmodeling of the modules and core of the caenorhabditis elegans connectome. *PLoS ONE* **9**, e97584 (2014).
47. Bassett, D. S. et al. Efficient physical embedding of topologically complex information processing networks in brains and computer circuits. *PLoS Comput. Biol.* **6**, e1000748 (2010).
48. Nieuwenhuys, R. et al. *The Central Nervous System of Vertebrates*. (Springer, 1997).
49. Suárez, L. E. et al. A Connectomics-Based Taxonomy of Mammals. *eLife* **11**, e78635 (2022).
50. Rueda-Alaña, E. & García-Moreno, F. Time in neurogenesis: conservation of the developmental formation of the cerebellar circuitry. *Brain Behav. Evol.* 1–15 https://doi.org/10.1159/000519068. (2021)
51. Arnatkeviciute, A., Fulcher, B. D., Bellgrove, M. A. & Fornito, A. Where the genome meets the connectome: understanding how genes shape human brain connectivity. *NeuroImage* **244**, 118570 (2021).
52. Sha, Z., Schijven, D., Fisher, S. E. & Francks, C. Genetic architecture of the white matter connectome of the human brain. *Sci. Adv.* **9**, eadd2870 (2023).
53. Lee, B. H., Smith, T. & Paciorkowski, A. R. Autism spectrum disorder and epilepsy: disorders with a shared biology. *Epilepsy Behav.* **47**, 191–201 (2015).
54. Ghacibeh, G. A. & Fields, C. Interictal epileptiform activity and autism. *Epilepsy Behav.* **47**, 158–162 (2015).
55. Stefanis, L. - Synuclein in Parkinson's disease. *Cold Spring Harb. Perspect. Med.* **2**, a009399–a009399 (2012).
56. Zarranz, J. J. et al. The new mutation, E46K, of α-synuclein causes parkinson and Lewy body dementia: new α-synuclein gene mutation. *Ann. Neurol.* **55**, 164–173 (2004).
57. Paul, K. C. et al. APOE, MAPT, and COMT and Parkinson's disease susceptibility and cognitive symptom progression. *JPD* **6**, 349–359 (2016).
58. Sidransky, E. et al. Multicenter analysis of glucocerebrosidase mutations in Parkinson's disease. *N. Engl. J. Med.* **361**, 1651–1661 (2009).
59. Cornell, R. SLC41A1 and TRPM7 in magnesium homeostasis and genetic risk for Parkinson?s disease. *J. Neurol. Neuromed.* **1**, 23–28 (2016).
60. Verghese, P. B., Castellano, J. M. & Holtzman, D. M. Apolipoprotein E in Alzheimer's disease and other neurological disorders. *Lancet Neurol.* **10**, 241–252 (2011).
61. Ulland, T. K. & Colonna, M. TREM2—a key player in microglial biology and Alzheimer disease. *Nat. Rev. Neurol.* **14**, 667–675 (2018).
62. Diaz-Lucena, D. et al. TREM2 expression in the brain and biological fluids in prion diseases. *Acta Neuropathol.* **141**, 841–859 (2021).
63. Cuccaro, M. L. et al. *SORL1* mutations in early- and late-onset Alzheimer disease. *Neurol. Genet* **2**, e116 (2016).
64. Harrington, A. J. et al. MEF2C regulates cortical inhibitory and excitatory synapses and behaviors relevant to neurodevelopmental disorders. *eLife* **5**, e20059 (2016).
65. Buddell, T., Friedman, V., Drozd, C. J. & Quinn, C. C. An autism-causing calcium channel variant functions with selective autophagy to alter axon targeting and behavior. *PLoS Genet* **15**, e1008488 (2019).
66. Claes, L. et al. De Novo mutations in the sodium-channel gene SCN1A cause severe myoclonic epilepsy of infancy. *Am. J. Hum. Genet.* **68**, 1327–1332 (2001).
67. Lagae, L. et al. Fenfluramine hydrochloride for the treatment of seizures in Dravet syndrome: a randomised, double-blind, placebo-controlled trial. *Lancet* **394**, 2243–2254 (2019).
68. Parenti, I., Rabaneda, L. G., Schoen, H. & Novarino, G. Neurodevelopmental disorders: from genetics to functional pathways. *Trends Neurosci.* **43**, 608–621 (2020).
69. Bassett, D. S. & Bullmore, E. T. Human brain networks in health and disease. *Curr. Opin. Neurol.* **22**, 340–347 (2009).
70. Levin, H. S. et al. Relationship of depth of brain lesions to consciousness and outcome after closed head injury. *J. Neurosurg.* **69**, 861–866 (1988).
71. Rolls, E. T., Huang, C.-C., Lin, C.-P., Feng, J. & Joliot, M. Automated anatomical labelling atlas 3. *NeuroImage* **206**, 116189 (2020).
72. Nowinski, W. L. Evolution of human brain atlases in terms of content, applications, functionality, and availability. *Neuroinform* **19**, 1–22 (2021).
73. Nieuwenhuys, R. & Puelles, L. *Towards a New Neuromorphology*. (Springer, https://doi.org/10.1007/978-3-319-25693-1.2016).
74. Nieuwenhuys, R. & Nieuwenhuys, R. Principles of current vertebrate neuromorphology. *Brain Behav. Evol.* **90**, 117–130 (2017).
75. Workman, A. D., Charvet, C. J., Clancy, B., Darlington, R. B. & Finlay, B. L. Modeling transformations of neurodevelopmental sequences across mammalian species. *J. Neurosci.* **33**, 7368–7383 (2013).
76. Glasser, M. F. et al. The minimal preprocessing pipelines for the human connectome project. *NeuroImage* **80**, 105–124 (2013).
77. Desikan, R. S. et al. An automated labeling system for subdividing the human cerebral cortex on MRI scans into gyral based regions of interest. *NeuroImage* **31**, 968–980 (2006).
78. Pauli, W. M., Nili, A. N. & Tyszka, J. M. A high-resolution probabilistic in vivo atlas of human subcortical brain nuclei. *Sci. Data* **5**, 180063 (2018).
79. Edlow, B. L. et al. Neuroanatomic connectivity of the human ascending arousal system critical to consciousness and its disorders. *J. Neuropathol. Exp. Neurol.* **71**, 531–546 (2012).
80. Oldham, S. et al. Consistency and differences between centrality measures across distinct classes of networks. *PLoS ONE* **14**, e0220061 (2019).
81. Zhang, Y., Brady, M. & Smith, S. Segmentation of brain MR images through a hidden Markov random field model and the expectation-maximization algorithm. *IEEE Trans. Med. Imaging* **20**, 45–57 (2001).
82. Burt, J. B., Helmer, M., Shinn, M., Anticevic, A. & Murray, J. D. Generative modeling of brain maps with spatial autocorrelation. *NeuroImage* **220**, 117038 (2020).
83. Shen, E. H., Overly, C. C. & Jones, A. R. The Allen human brain atlas. *Trends Neurosci.* **35**, 711–714 (2012).
84. Arnatkevičiūtė, A., Fulcher, B. D. & Fornito, A. A practical guide to linking brain-wide gene expression and neuroimaging data. *NeuroImage* **189**, 353–367 (2019).

85. Zhou, Y. et al. Metascape provides a biologist-oriented resource for the analysis of systems-level datasets. *Nat. Commun.* **10**, 1523 (2019).
86. Piñero, J. et al. The DisGeNET knowledge platform for disease genomics: 2019 update. *Nucleic Acids Res.* gkz1021 https://doi.org/10.1093/nar/gkz1021.(2019)
87. Fulcher, B. D., Arnatkeviciute, A. & Fornito, A. Overcoming false-positive gene-category enrichment in the analysis of spatially resolved transcriptomic brain atlas data. *Nat. Commun.* **12**, 2669 (2021).

Acknowledgements

We thank M. De Pittá, D. Papo, D. Marinazzo, A. Mazzoni, Y. Ben-Ari for helpful suggestions and critical comments. **Funding**. Authors declare that they have no competing interests. ANR was supported by grant PID2022-139237NB-I00 funded by MCINAEI/10.13039/501100011033 and "ERDF A way of making Europe". PB acknowledges financial support from Ikerbasque (The Basque Foundation for Science) from FEDER (grant SAF2015-69484-R and AI-2021-039), from Ministerio de Ciencia, Inovación e Universidades of Spain (MICINN grant, PID2021-127163NB-I00, funded by the MCIN/AEI/10.13039/501100011033/FEDER, UE) and from EITB-Maratoia (Project number BIO22/ALZ/010/BCB funded by Dep Salud of the Government of the Basque country and BIOEF. FGM is supported by Ikerbasque, and holds Spanish Ministry MICINN PGC2018-096173-A-I00 and PID2021-125156NB-I00 grants and a Basque Government PIBA_2022_1_0027 grant. JMC acknowledges financial support from Ikerbasque: The Basque Foundation for Science, and from Spanish Ministry of Science (PID2023-148008OB-I00), Spanish Ministry of Health (PI22/01118), Basque Ministry of Health (2023111002 & 2022111031). ID was supported by Ikerbasque Research Fellow and Spanish Ministry of Science (RYC2022-035429-I and PID2023-150633OA-I00)

Author contributions

Conceptualization: F.G.M. and P.B. Methodology: I.D., F.G.M., N.C.S., S.S., A.N.R., M.D.A., J.M.C., and P.B. Writing – original draft: F.G.M., I.D., M.D.A., J.M.C., and P.B. Funding acquisition: F.G.M., J.M.C., and P.B.

Competing interests

The authors declare no competing interests.

Additional information

Supplementary information The online version contains supplementary material available at https://doi.org/10.1038/s41467-025-67785-3.

Correspondence and requests for materials should be addressed to Paolo Bonifazi.

Peer review information *Nature Communications* thanks the anonymous reviewers for their contribution to the peer review of this work.